Acta Materialia 117 (2016) 333–344

Contents lists available at ScienceDirect

Acta Materialia

journal homepage: www.elsevier.com/locate/actamat

Full length article

Microstructurally sensitive crack nucleation around inclusions in powder metallurgy nickel-based superalloys

J. Jiang [a, b, *], J. Yang [c], T. Zhang [a, 1], J. Zou [c], Y. Wang [c], F.P.E. Dunne [a, b], T.B. Britton [a]

[a] Department of Materials, Imperial College London, UK
[b] Department of Mechanical Engineering, Imperial College London, UK
[c] Science and Technology on Advanced High Temperature Structural Materials Laboratory, Beijing Institute of Aeronautical Materials, Beijing 100095, China

ARTICLE INFO

Article history:
Received 8 July 2016
Accepted 12 July 2016

Keywords:
High-resolution digital image correlation
High-resolution electron backscatter diffraction
Crack nucleation
Non-metallic inclusion

ABSTRACT

Nickel-based superalloys are used in high strength, high-value applications, such as gas turbine discs in aero engines. In these applications the integrity of the disc is critical and therefore understanding crack initiation mechanisms is of high importance. With an increasing trend towards powder metallurgy routes for discs, sometimes unwanted non-metallic inclusions are introduced during manufacture. These inclusions vary in size from ~10 μm to 200 μm which is comparable to the grain size of the nickel-based superalloys. Cracks often initiate near these inclusions, and the precise size, shape, location and path of these cracks are microstructurally sensitive. In this study, we focus on crack initiation at the microstructural length scale using a controlled three-point bend test, with the inclusion deliberately located within the tensile fibre of the beam. Electron backscatter diffraction (EBSD) is combined with high spatial resolution digital image correlation (HR-DIC) to explore full field plastic strain distributions, together with finite element modelling, to understand the micro-crack nucleation mechanisms. This full field information and controlled sample geometry enable us to systematically test crack nucleation criteria. We find that a combined stored energy and dislocation density provide promising results. These findings potentially facilitate more reliable and accurate lifing prediction tools to be developed and applied to engineering components.

1. Introduction

Turbine discs are safety critical components in modern aero engines and are typically made from nickel-based superalloys. Powder metallurgy routes are employed for these components as this enables precise microstructure control, which is required to extract optimal performance, typically focussing on high strength and excellent damage tolerance with minimal component weight [1]. Unfortunately, this manufacturing route can introduce non-metallic ceramic inclusions during the powder generation and handling processes which are often between of 10 μm–200 μm and occasionally found with the nickel powder particles. The inclusions are introduced from the refractory crucible materials which are used to produce the alloy, such as the primary vacuum induction melt ingot, the secondary vacuum induction melt ingot, guide tube arrangement for the atomization stream and reactions between the molten stream and the gases in the atomization chamber [2]. Although every effort has been made to filter them, complete removal from the final products is difficult to achieve [1].

Discs are operated in the extreme environment of a gas turbine, often at elevated temperatures (650 °C –800 °C) and undergo severe cyclic loading. The typical failure mode is fatigue [3] and for powder metallurgy (PM) alloys, often fatigue crack initiation begins at these non-metallic inclusions, which reduces component life by 100 times [4,5]. Simple correlations exist that indicate the importance of these inclusions, such as those between size and life debit [2,5–7]. However, a full mechanistic understanding of crack initiation and microstructurally sensitive short crack growth has yet to be achieved [8–13]. This lack of understanding inhibits further development of physically-based models that can be employed to design new materials and enhance component life.

Microstructurally sensitive crack nucleation related to non-metallic inclusions is not limited to PM nickel-based superalloys for aeroengine applications, as these issues are shared with weld steels [14,15] and aluminium alloys [16]. Therefore generation of

* Corresponding author.
E-mail address: jun.jiang@imperial.ac.uk (J. Jiang).
[1] Current address: Worcester Polytechnic, MA, USA.

http://dx.doi.org/10.1016/j.actamat.2016.07.023

physically based understanding, rather than empirical curve-fitting, enhances our ability to realise microstructure engineering for enhanced fracture resistance [17] across a range of materials systems and component applications. This study focuses on the ceramic inclusion existing in PM nickel-based superalloy. This can be related to prior work which has focussed on oxide (hard and brittle) or carbide (relatively ductile) inclusions [2]. The inclusion in this work is highly porous and hollow structure, which may generate significant differences in the associated damage and fatigue crack initiation mechanisms as compared with the prior work.

This manuscript builds on our prior work in the area of non-metallic inclusions and fatigue crack initiation in nickel-based superalloys [18,19]. Highlights pertinent to the current work include observations that the distribution and evolution of geometrically necessary dislocation (GND) density and large Type III (intra-granular) residual stresses, both measured using high angular resolution EBSD, are correlated with microstructure around the non-metallic inclusion during deformation under three-point bending in a low cycle fatigue test [18]. The patterning of stored GND density and residual stresses were found to be developed during the first cycle. The evolution of these patterns under subsequent cycles did not substantively change the structure of these deformation patterns. These observations were limited to cyclic fatigue around an inclusion in one PM alloy within a small region (~20 grains), as a result of the experimental difficulty and time (>100hr microscopy time for 16 observations). Furthermore, this study only focused on residual deformation with a diffraction based technique and so correlations with accumulated plastic slip were impossible. A sister study by Zhang et al. [20] focussed on fatigue crack nucleation near a different non-metallic inclusion in an alternative nickel-based superalloy, this time employing conventional EBSD with high spatial HR-DIC. Zhang noted that there was significant microstructural sensitivity towards the range of accumulated local plastic strains, which was further modelled by Zhang et al. [19] with Crystal Plasticity Finite Element Analysis (CP-FEA). In the latter work, the use of integrated crystal modelling with HR-DIC studies local to the non-metallic inclusions showed that a key defect nucleation mechanism was that of interfacial nickel/oxide decohesion and the interfacial decohesion strength was quantified.

These two prior studies highlight two sides of experimental characterisation: Jiang et al. [18] focus on the stored energy problem, associated with residual stress and local hardening due to GND density; whereas Zhang et al. [20] focus on plastic slip, and therefore energy dissipation due to plastic work near the inclusion. Both of these processes are microstructurally sensitive.

In the present work, we combine experimental micro-mechanical characterisation with HR-EBSD, at the initial and final states, together with HR-DIC captured periodically during mechanical testing, to enable us to assess microstructural evolution during cyclic loading. The nickel-based superalloy near the inclusion has been found to crack, and we used knowledge of the stored GND density (from EBSD) and accumulated plastic strain (from HR-DIC) to test a previously postulated crack nucleation criterion [18]. This experimental study is supplemented with a geometrically faithful finite element model to illustrate the relative importance of inclusion/matrix shape on crack nucleation.

2. Methodology

A 3 mm × 3 mm × 12 mm cuboid nickel-based superalloy FGH96, provided by AVIC-BIAM, was carefully cut to contain the inclusion within the tensile fibre of the bend specimen, as indicated in Fig. 1 (a). Prior to testing, the sample was annealed at 750 °C for 7 h to stress relieve the microstructure and reduce any stored energy. The sample was metallographically prepared using silicon carbide papers down to P4000 grit and subsequently polished with a 0.05 μm colloidal silica slurry for 40 min to remove the residual mechanical damage introduced during sample preparation process, making it suitable for EBSD characterisation and our study.

To capture the initial microstructure around the non-metallic inclusion, a 165 μm × 125 μm EBSD map with 0.25 μm step size at x1000 magnification was obtained using a Bruker e⁻FlashHR detector and Quantax ESprit 2.0 system. A 25 keV accelerating voltage and 16 nA probing current were applied in a Zeiss Auriga SEM. The measured local microstructure near the non-metallic inclusion is revealed by the IPF map (plotted with respect to the loading direction) in Fig. 1(b). The inclusion is shown as a black unindexed area at the centre of the map. The surrounding nickel-based superalloy matrix is a typical polycrystalline microstructure, including a large fraction of annealing twins. The sample was made using a powder metallurgy route and therefore, as expected, there is no significant texture in this area. The average grain size is approximately 6 μm.

2.1. Mechanical test

Mechanical testing was performed using interrupted cyclic three point bending, with the rig illustrated in Fig. 1 (a). The test was run in displacement control, prescribing the position of the

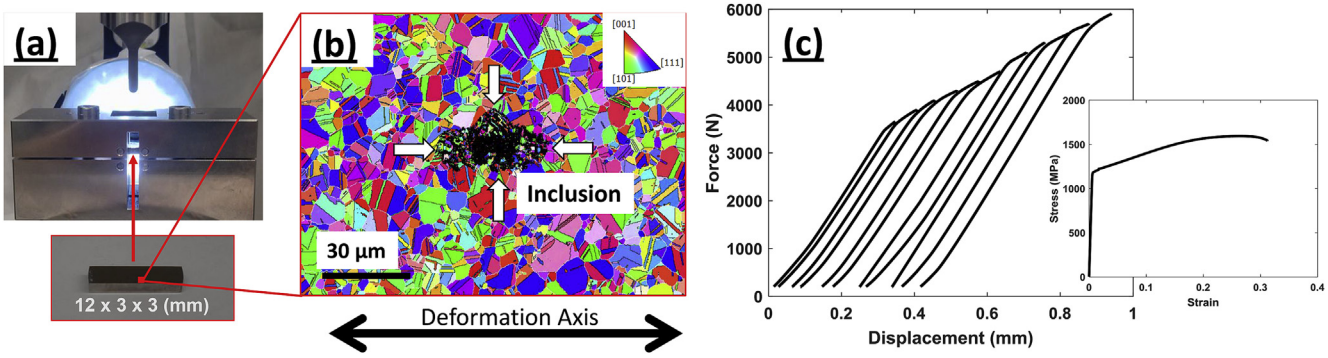

Fig. 1. (a) The experimental three-point bending test set up. The vertical force was applied from the top, and the dimension of the specimen is 12 mm × 3 mm × 3 mm, shown in the insert. The sample was machined to contain the inclusion within the tensile fibre of the bend specimen, indicated with the red box in the insert; (b) the EBSD measured inverse pole figure (IPF) map with respect to the deformation axis (the horizontal one). The inclusion is shown as the unindexed region at the centre of the map, highlighted with white arrows; (c) the measured applied force and cross head displacement curves. The inset showing the macroscopically measured true stress-strain curve of FGH96 alloy under a uniaxial tensile test. (For interpretation of the references to colour in this figure legend, the reader is referred to the web version of this article.)

crosshead attached to the central roller. A feedback loop was used to load the sample with a loading rate of 100 N/s. For each cycle the load was increased. After each target load had been applied, the sample was unloaded at the same loading rate, removed from the mechanical test frame, and inserted into the SEM for SEM imaging for HR-DIC or for EBSD measurements. The first cycle was loaded to 3650 N, and a simple elastic finite element model indicates that this is beyond the yield stress in the maximum tensile fibre of the beam (i.e. where the inclusion was located). The applied load as a function of the displacement of loading point is plotted and shown in Fig. 1 (c). Repeated tests were conducted with a load increment of 200 N until the load reached 5900 N, at which points cracks were directly observed at several places local to the inclusion. A pronounced work hardening process can be observed in Fig. 1 (c). Due to the practical difficulties to place the sample back to the same position in the testing rig, the load and displacement curves obtained are not evenly distributed. However, progressively increasing plasticity at the macro-scale is clear.

2.2. Plastic deformation measurement

DIC is a cross-correlation based method which tracks local displacements between regions extracted two pairs of images. We utilised in-house code written in Matlab that implements cross-correlation of multiple regions of interest with sub-pixel precision [21]. As this technique has been available for several decades, the fundamental mathematical framework can be found elsewhere [22]. The detailed description of our Matlab-based DIC code can be found in a previous publication [23]. The total surface strain fields are then calculated from numerically differentiating the surface displacement field. The strain components were determined using continuum mechanics theory. The in-plane deformation gradients F were calculated by determining the gradient of displacement field (a numerical derivation using three points along the horizontal and vertical axes respectively), which is described by a quadratic polynomial fitting function. The Green-Lagrange strain tensor E is determined by Eq. (1).

$$\boldsymbol{E} = \frac{1}{2}\left(\boldsymbol{F}^{\mathrm{T}}\boldsymbol{F} - \boldsymbol{I}\right) \tag{1}$$

where the I is the identify tensor, T is a matrix operation to transpose the matrix F.

In this study, the cross-correlation was carried out by comparing the test image with the previous image (i.e. n with n-1). The ultimate displacement field, used for strain calculations, was used based upon summing the total accumulated displacement from each test image to the initial one.

For the HR-DIC method, it is critical to have high contrast SEM images at high magnification. Previously the authors found that nano-sized silica particles could be used as a very good system for HR-DIC measurement [20,23]. We note that there are other promising surface coating methods, such as self-assembling gold particles [24], etching the intrinsic microstructure features [25], gold remodelling [26]. The polishing liquid containing the average size of ~250 nm silica particles was diluted with distilled water at a ratio of 1:8. The solution was thoroughly mixed by putting it in an ultrasonic bath for 20 min. A drop of the mixture was carefully put at the region ROI of the sample surface. To avoid the breaking away of silica particles in a vacuum condition in a SEM, the sample was left to dry on a hot plate at an elevated temperature of 250 °C for 3 min. The sample surface was inspected frequently under an optical microscope until a relatively uniform distribution of particles was achieved.

The sample was then moved into a SEM, and an example micrograph is shown in Fig. 2. The SEM images were captured at a moderate magnification (x1000 on this instrument). In order to minimise the SEM drifting and distortion problems, the sample was left in the SEM for at least 40 min to allow the electron beam to stabilise before acquiring a SEM images. Furthermore, 3 scanning lines were averaged to reduce the SEM distortions and noise. Each 3072 pixel x 2304 pixel and 8-bit depth image, captured with a 55 nm pixel size, took ~3–4 min to ensure the high image quality to be achieved. At the end of the test, to acquire a final state HR-EBSD map, the sample was emerged in acetone solution for 24 h. The surface DIC coating was then removed by putting the sample in an ultrasonic bath for 1 h.

The subsets of a size of 100 × 100 pixel and 90% subset overlap were used for the cross-correlation analysis. Thus a nominal 0.6 μm spatial resolution was achieved. The nominal strain measurement sensitivity was estimated as 0.1% as shown in Zhang et al. [20]. It should be noted that the DIC measurement was conducted at the un-loaded state, and hence it characterized the residual plastic deformation state of the sample.

2.3. GND density measurement

Plastic deformation of metals is typically accommodated by dislocation motion. The progress of slipping dislocations through

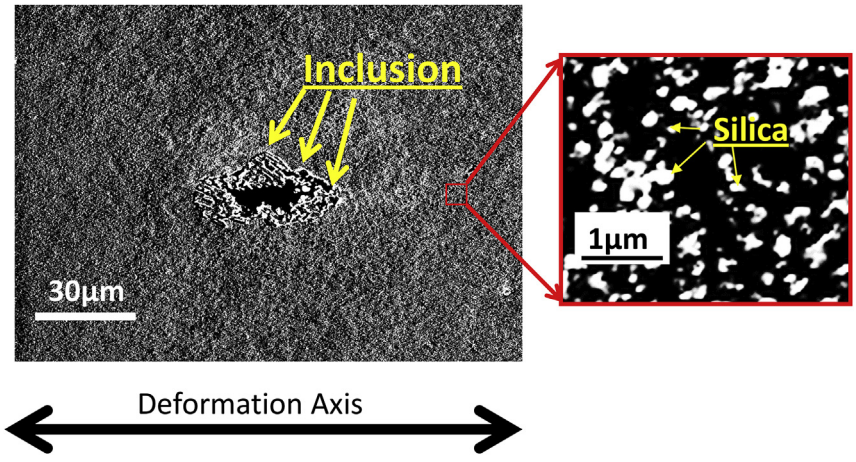

Fig. 2. SEM micrographs of the region of interest coated with the silica speckle pattern for HR-DIC measurements. The central object is the non-metallic inclusion. The sample was imaged at a working distance of 5 mm, with line averaging and a reasonable dwell time. The insert shows the nano-sized silica particles used for DIC tracking (contrast has been augmented for clarity).

the material controls mechanical properties, such as yield, working hardening and crack nucleation. At the microscale, dislocation activity can be observed from: (a) total strain of the material for the unloaded state, as measured with HR-DIC, if accommodated by plastic slip; (b) stored dislocation density, often split into statistically stored dislocations (SSDs) and GNDs [27]. Both SSDs and GNDs are related to work hardening [28,29] but their nucleation and local contributions [20] are subtly different: GNDs arise due to particular plastic strain gradients [30–32]; whereas SSDs (e.g. dislocation dipoles) are thought to evolve as a function of total plastic strain [33,34].

In this study, we employ HR-EBSD that measures lattice rotations with very high precision (1×10^{-4} rad [35]) and calculated two spatial gradients of the lattice rotation tensor (containing three terms) thus yielding six measured curvatures. While in theory all dislocations are geometrically necessary (e.g. if the Burgers circuit just contains half of a dipole), from an experimental perspective the size of the Burgers circuit is related to the EBSD step size (0.25 μm) and spatial derivate employed (our method is described in more detail here [36]). Furthermore, we note that the measurement of GND density with 2D EBSD maps is founded upon five components and one difference of the Nye tensor, and therefore the step size of the EBSD map is important [37]. In this work the fcc nickel-based superalloy considered has 18 <111> {110} dislocation types [38], which are separated into the pure edge and screw components. As only 6 input constraints are known and there are more potential dislocation types, we choose an 'L1 minimisation' solution that weights according to the minimum line energy (a more detailed description of this approach as applied to nickel-based superalloys can be found elsewhere [39]).

3. Results

3.1. Micro-crack nucleation

Six micro-cracks were observed to have formed around the non-metallic inclusions (as shown in Fig. 3 (a)). These cracks are short, extending from the inclusion only within one or two grains. The SEM micrograph (Fig. 3 (a)) also shows a clear indication of surface slip traces. The crack paths are often parallel with slip traces within the same grains (i.e. they are microstructurally sensitive short cracks). Evaluation of the position and extent of these cracks with respect to the EBSD IFP map (Fig. 3 (b)) reveals that the microstructurally sensitive cracks are both intragranular and intergranular. Furthermore, it is worth noting that despite significant plasticity occurring around the inclusion and near the crack tips, the quality of the EBSD data in this area remains high. This will be explored in more detail with the HR-EBSD analysis in the next section. It is likely that there are some small nickel grains embedded within the inclusion, due to the highly porous structure of the inclusion. This inclusion also has a hollow structure, with a large void in the central region.

It can be seen in Fig. 4 that no obvious cracking was observed in the first few loading cycles. The agglomerate inclusion contains many and widespread pores, as highlighted in Figs. 3 (a) and 4 (a), and was found to fracture at 4900 cycles. The presence of the pores is argued to have a substantive effect on the effective agglomerate stiffness, to the extent that both tensile and compressive stress loading results in a more compliant response than the surrounding nickel matrix. The cohesive strength between agglomerate and nickel is sometimes found to be low, but with respect to the pore-filled agglomerate studied in this work, its reduced isotropic stiffness is likely to preclude decohesion as a failure mechanism since the interfacial stresses will, as a consequence, remain low. Hence, it is reasonable to assume that it behaves elastically and with a lower stiffness than the surrounding Ni matrix. Several cracks highlighted in Fig. 4 have developed within the nickel matrix. With increasing loading, an additional three cracks have become very apparent by 5700 cycles.

3.2. The overview of microstructure, strain and GND density

The microstructure, effective strain and GND density maps before and after the three-point bending test are illustrated in Fig. 5.

EBSD mapping before and after the test reveals that grain morphology and orientation in the strained region did change significantly as a result of the plastic deformation associated with the bend test, as revealed in Fig. 5(a) and (d).

The accumulation of plastic strain in this region is very heterogeneous, as shown in Fig. 5(b) and (e). Regions of significant in plane strain are located typically at +/− 45° to the tensile axis, as expected, but this field is heavily modulated by the presence of the inclusions and particular grain combinations within the deforming region. From observation of the series of HR-DIC maps, plasticity was observed to initiate at the inclusion (~1% strain) and some

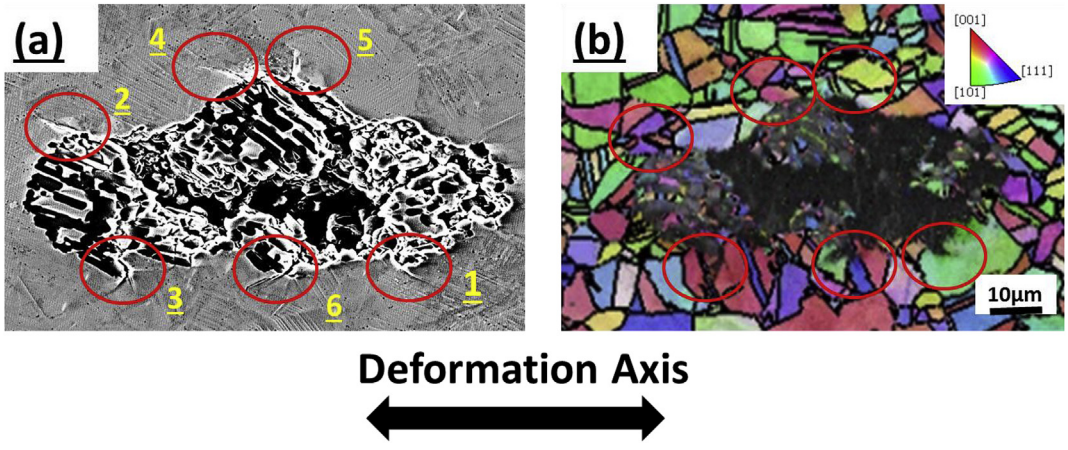

Fig. 3. he nucleation of micro-cracks around the non-metallic inclusion after 5900 N. Six micro-cracks highlighted within the red ellipses (a) SEM micrograph, (b) corresponding EBSD IPF map, generated with respect to the major deformation axis in the tensile fibre of the three point bend test. (For interpretation of the references to colour in this figure legend, the reader is referred to the web version of this article.)

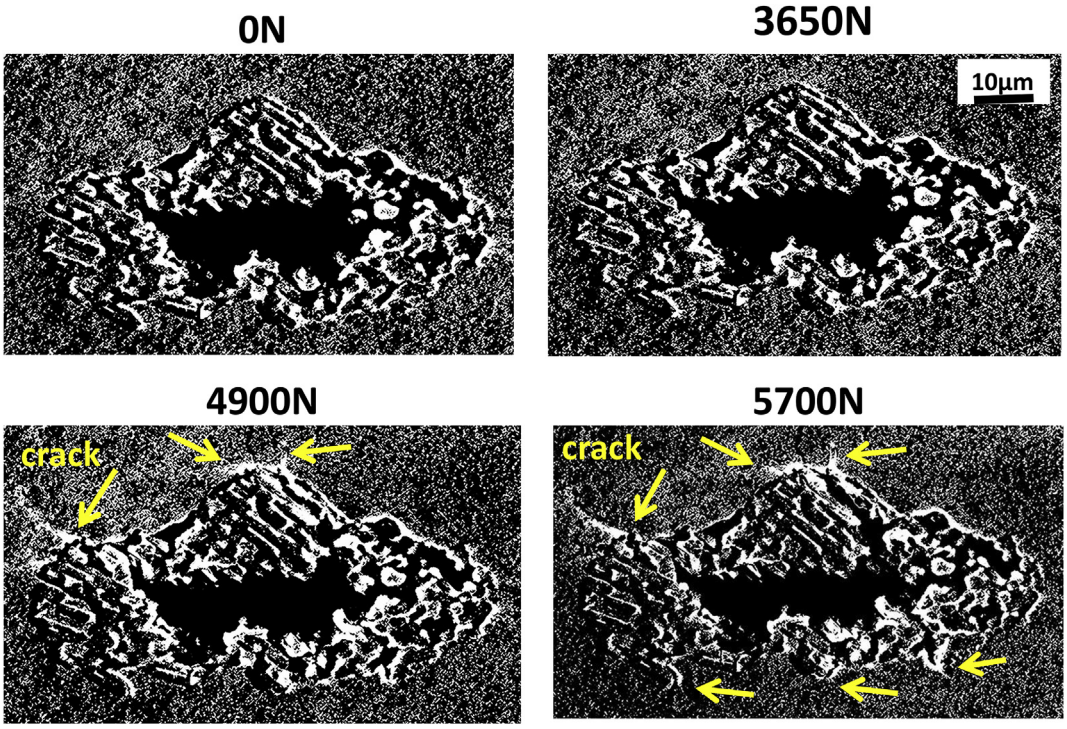

Fig. 4. btained SEM images show the crack locations and opening process with increasing load at 0 N, 3900 N, 4900 N and 5700 N respectively. Crack locations are highlighted with yellow arrows. (For interpretation of the references to colour in this figure legend, the reader is referred to the web version of this article.)

other particular grains local to but removed from the inclusion. As the load increases, the two ~45° 'butterfly-shaped' deformation bands were generated with the strongest strain localisation occurring adjacent to the inclusion. Each of these bands of high strain localisation is connected with the inclusion.

Note that DIC utilises the measurement of surface in-plane displacements to calculate strains and therefore the opening of cracks can also lead to large values of (apparent) in-plane effective

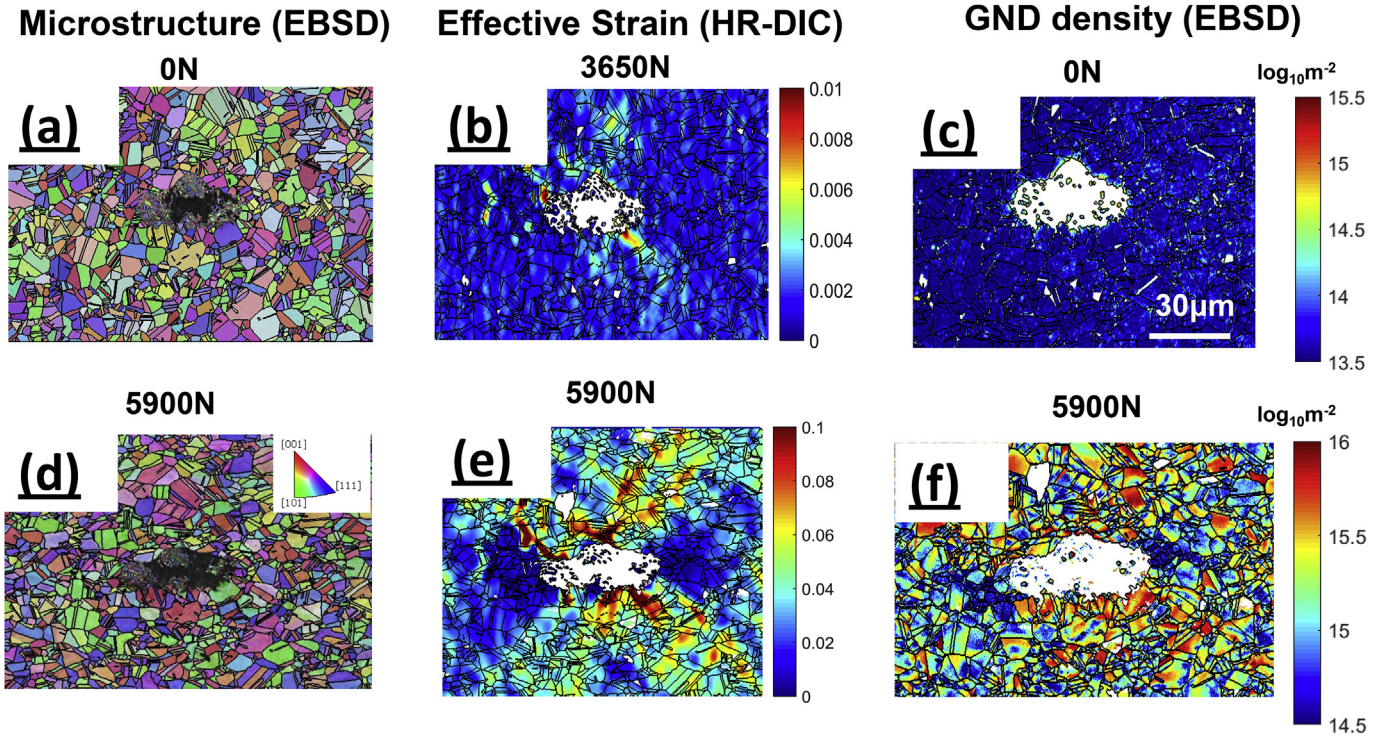

Fig. 5. (a) and (d) showing the EBSD measured initial (0 N) and final (5900 N) IPFs with respect to the deformation axis. (b) and (e) revealing the distribution of (in-plane) effective strain at 3900 N (beginning of plasticity) and 5900 N (final loading step) respectively:, which was measured by HR-DIC method. The effective strain map was overlaid with EBSD measured grain boundary map. The location of the inclusion was used as the fiducial mark to ensure the accurate position of grain boundary network. (c) and (f) illustrating the lower bound estimated GND density maps of the undeformed (0 N) and cracked states (5900 N) respectively.

strain. However, as a series of images were captured during this test it was possible to track strain levels prior to the observation of surface cracks in the sister SE micrographs.

After heat treatment and prior to deformation, on average low dislocation content (5.6×10^{12} lines/m^2 with the step size of 0.25 μm) is observed, see Fig. 5 (c). However some dislocations can still be found near the interface between the inclusion and nickel matrix due to different thermal expansion (this has been observed previously [40]). In the final state, as seen in Fig. 5 (f), the overall GND density increased significantly and pronounced spatial variations are also observed. Superficially, there are many grains with high GND density (>10^{15} lines/m^2) immediately above and below the inclusion. Grains immediately to the left and right of the inclusion, i.e. in series within that particular tensile fibre, show very little accumulation of GND density. These observations must be considered in light of significant variations in GND density throughout the entire map.

3.3. Strain distribution and development

There is a progressive evolution of the in-plane effective strain in the region surrounding the inclusion, as shown in the highlighted 4 (of 13) HR-DIC derived maps shown in Fig. 6. The heterogeneous nature of the plastic strain is revealed very early in this deformation series, e.g. at 3650 N in Fig. 6 (a). With increasing load, strain localisation progressively expands away from the inclusion and the 'butterfly' shape starts to develop. The pattern of the butterfly tends to increase in contrast, indicating that strain continues to localise within these particular microstructural units, rather than spread more homogeneously throughout the Ni matrix.

Further observation of the sister SEM micrographs (used to generate the DIC strain maps) indicates that the cracks were nucleated prior to 4900 N (note that SEM imaging is performed in the unloaded configuration, and so the cracks have to be sufficiently open in order for them to be observed in each SEM micrograph).

This HR-DIC is a quantitative assessment of the strain in the studied region and is ripe for quantitative statistical analysis. Evolution of the mean and range of the in-plane effective strain distribution is revealed Fig. 6 (c). As expected, the mean strain increases with progressive loading. Furthermore, the range of strain values continues to develop, confirming qualitative assessment that regions of high strain tend to develop faster than regions of low strain, as indicated by increasing development of contrast within the butterfly. Three distributions have been plotted as full histograms in Fig. 6 (f) which shows that these distributions start off near Gaussian and progressively evolve into a skew distribution with a large high strain tail. It should be noted that the strain measurement at the head of the cracks is not precise, as the displacement field consists not only of displacements due to plastic strain but also the crack opening displacements. Furthermore, where these displacements are very large, the cross-correlation fails (due to a lack of image similarity).

3.4. Correlative assessment of crack tips

Five (of six) micro-cracks are focussed on here to reveal correlative insight into local deformation patterning and microstructure in Fig. 7:

Crack 1 – An intragranular crack extending along a particular microstructural plane [111] (along slip line), in a region of high effective strain and terminating in a region of high GND density.
Crack 2 – An intergranular crack extending along a straight coherent twin boundary in a region of high effective strain with high GND density in the two neighbour grains.
Crack 3 – An intergranular crack that extends from a grain boundary within a large grain containing many GNDs, and the crack is perturbed into a region of high in-plane effective strain.
Cracks 4&5 – two of several very small cracks that extend from the inclusion along grain boundaries one grain away in a region of high in-plane effective strain and high GND density.

Accumulated plastic slip, manifested in the in-plane effective strain maps, is a direct precursor to crack nucleation, as all five

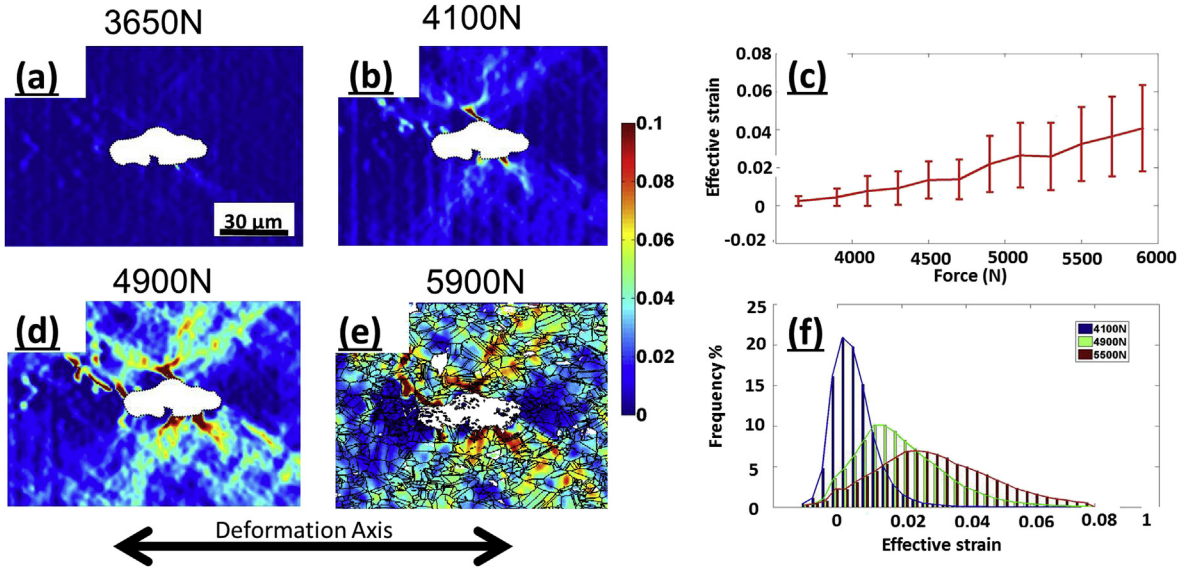

Fig. 6. The evolution of strain, as measured with HR-DIC, as a function of load during the interrupted three point bend test: (a), (b), (d) and (e) spatial distributions of the in-plane effective strain at the inclusion as a function of increasing load, at 3650 N, 4100 N, 4900 N and 5900 N respectively; in (e), the effective strain map is overlaid with grain boundary skeleton measured by EBSD for the final loading state (FIGURE XX), using the geometry and location of the inclusion as a fiducial mark to align these two maps. (c) shows statistical analysis of effective strain distribution and development as a function of load. Each error bar represents the distribution of all probed points in each strain map. The spread of the data (5% and 95%) is indicated by the width of error bar, and the mean values of maps (50%) are plotted as a curve. Three examples of detailed strain distribution are plotted as a histogram and shown in (f).

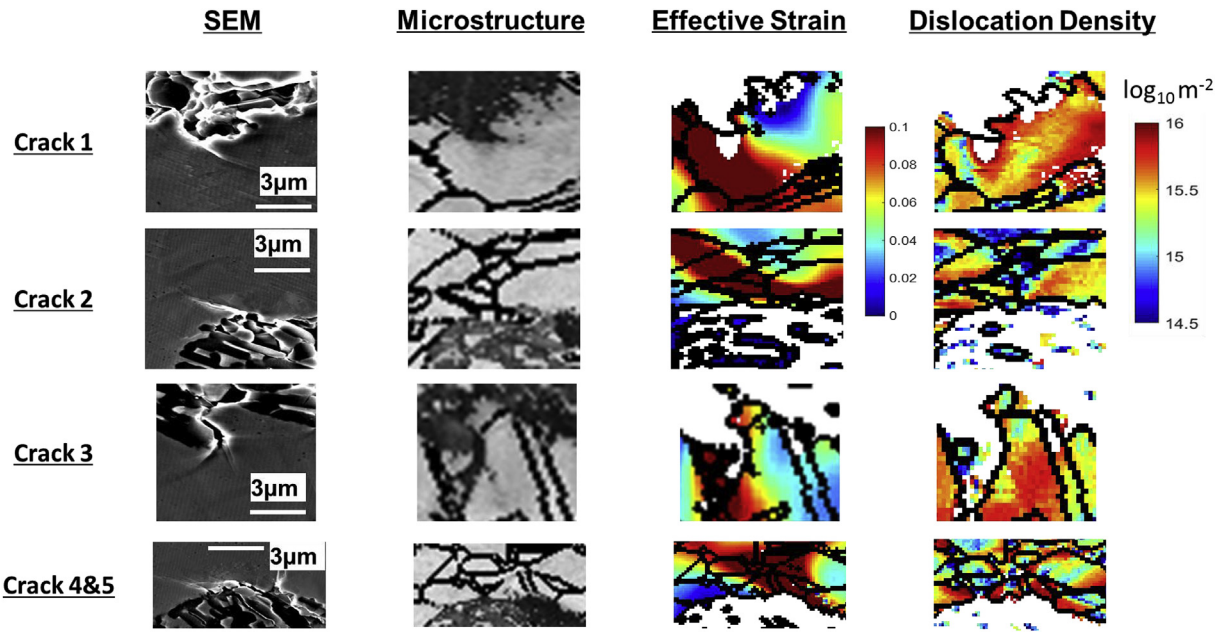

Fig. 7. Focused observation of the regions surrounding five of the cracks which initiate close the inclusion closer views: secondary electron micrographs (after 5900 N); microstructure as revealed using the 'image quality' EBSD metric and grain boundaries highlighted in black (after 5900 N); effective strain as extracted from the HR-DIC measurements (initial compared with 5900 N); and GND density measured using HR-EBSD (after 5900 N).

cracks emerge in regions of high strain in Fig. 7. However, there are also many regions of high strain around the inclusion where cracks do not form, and therefore there must be other factors involved. Potentially this is related to regions of high GND density ahead of the crack tips indicating that the nucleation of dislocation walls is likely also to play a significant role.

3.5. Crack forming criteria

The top 10% of strain at the end of the test is highlighted in Fig. 8(a). The crack nucleation sites clearly have a strong correlation with the strain hot spots. This is also confirmed by the top 10% strain maps at 3650 N as shown in Fig. 8(b), at which no cracks were presented. For the effective strain development shown in Fig. 6, for the majority of the probed points, the assumption of constant strain patterning throughout the experiment is reasonable, though slight strain variations can still be found between these two maps. The highest strain points are spread around the inclusion. However, in Fig. 8(a) and (b), it is very intriguing to note that there are some sites far from the inclusion, which have high strain, but do not generate any crack nucleation.

Stroh [41] argued that the crack nucleation is led by dislocation

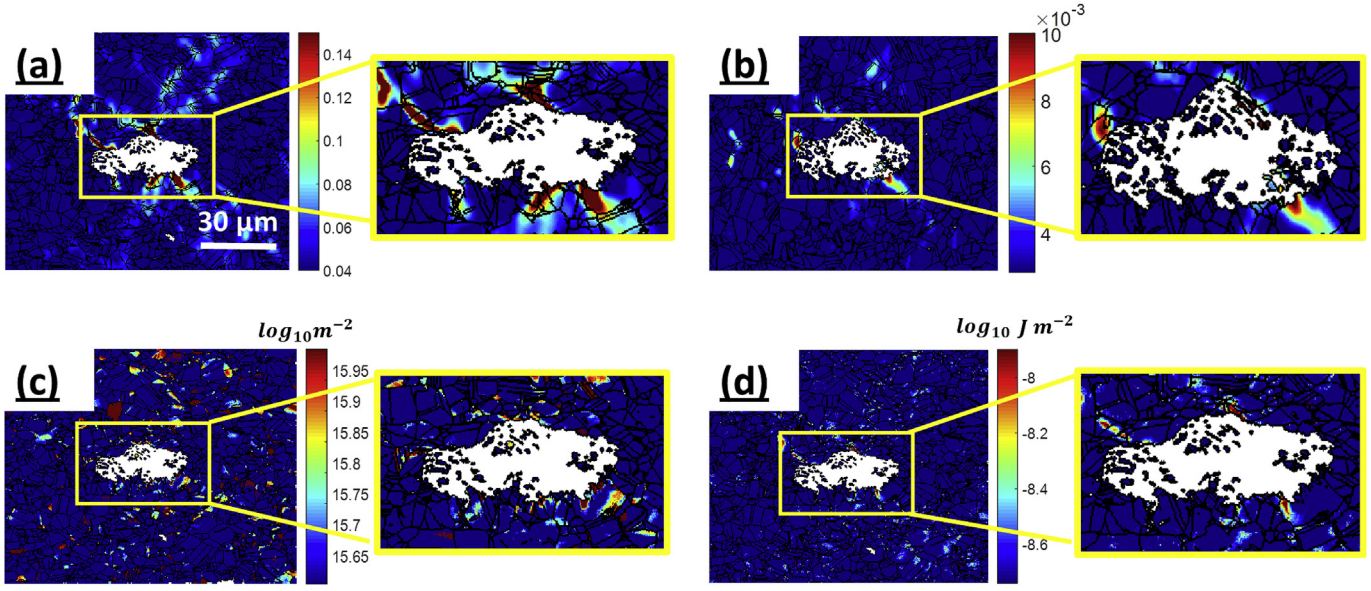

Fig. 8. Evaluation of the strain, GND and stored energy fields to generate understanding of crack nucleation mechanisms: (a) and (b) shows the locations of 'hot' (top 5% - indicated through tailoring of the colour scale) in-plane effective strain spots at 5900 N and 3650 N respectively, with overlay of grain boundaries from EBSD measurements; (c), the hot spots (top 5%) of GND density map, in dislocations per m2; (d) distribution of the hot spots (top 5%) of local stored energy density at log10 scale according to Eq. (4).

pile-up, as these dislocations increase the local shear stress and this enables nucleation of a micro-crack. The highlighted GND map shown in Fig. 8 (c) reveals that regions, where cracks are generated are correlated with high GND density, but that not all regions of high GND density are found at either the inclusion or where cracks have formed.

Dunne et al. [19,42,43] recently proposed a stored energy density criterion for fatigue crack nucleation, which considers the locally stored energy rate (per loading cycle) developed over an area determined by the local dislocation content in order to define the appropriate length scale with which to define the energy density. It therefore recognises the importance of (Griffith-like) stored energy and dislocation density (Stroh's model). They considered storage volume ΔV, written in terms of SSD and GND density, which is given by

$$\Delta V = \frac{\Delta A}{\sqrt{\rho_{SSD} + \rho_{GND}}} \tag{2}$$

The stored energy per cycle within the volume is then determined to be

$$W = \oint \left| \frac{\xi \boldsymbol{\sigma} : d\boldsymbol{\varepsilon}^p \Delta A}{\sqrt{\rho_{SSD} + \rho_{GND}}} \right. \tag{3}$$

where ξ is the fraction of the dissipated energy stored in the establishment of dislocation structure, and the integration is carried out over a complete loading cycle. The stored energy rate per cycle is then given by

$$\dot{G} = \frac{W}{\Delta A} = \oint \frac{\xi \boldsymbol{\sigma} : d\boldsymbol{\varepsilon}^p}{\sqrt{\rho_{SSD} + \rho_{GND}}} \tag{4}$$

To simplify Eq. (4) in order to enable an indication of the stored energy rate to be estimated from our experimental observations, the stress is assumed to be constant since the local microstructural stress around a given cyclic hysteresis loop is not known. In addition, as it is generally accepted that the density ρ_{SSD} is proportional to the applied plastic strain ε [44], only the GND density is considered here and is argued to have the stronger influence on the distribution of stored energy density. The Eq. (5) is used in our analysis simply to be approximately indicative of the local stored energy density. The stored energy density map so determined is shown in Fig. 8 (d).

$$\dot{G} = \oint \frac{\boldsymbol{I} : d\boldsymbol{\varepsilon}^p}{\sqrt{\rho_{GND}}} \tag{5}$$

3.6. The relationship between strain and GND density

In this study, we are fortunate to obtain both strain and GND density maps at the same region, and it is useful to study the relationship between these two quantities. Clearly, as shown in Fig. 5(e) and (f), the distributions of strain and GND density are very different. A further statistical analysis to evaluate the correlation between these quantities is revealed in Fig. 9. High strain locations tend to have high GND density associated with them. However, only a small fraction of high GND density points is associated with high strain values. The majority of high GND density points have relatively small strain.

3.7. Geometrical effects of the inclusion

To study the first order geometrical effects of the inclusion on

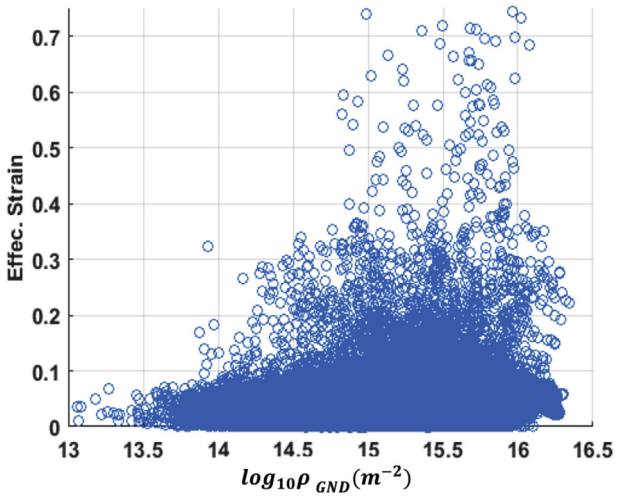

Fig. 9. A scatter plot of effective strain as a function of grain averaged GND density at log10 scale. Data points were extracted from the final GND density and strain maps (5900 N).

stress distributions, an isotropic elastic finite element (FE) model was built, in which the geometry of the inclusion was carefully drawn and embedded in an isotropic nickel matrix. No further explicit microstructure was modelled in this case. The inclusion is assumed to be less stiff than the nickel matrix. This model reveals that the distribution of maximum shear stress is strongly influenced by the shape of the inclusion, shown in Fig. 10 (a). These geometrically induced variations in local stress state are reflected in the regions of high strain, shown in Fig. 10 (b), and eventual crack initiation sites (see section 3.1). The most striking correlation here is that regions of low shear stress, to the left and right of the inclusion, are reflected in the regions of low in-plane effective strain.

While this first order geometrically faithful elastic analysis clearly provides some significant hints at where strain will localise around non-metallic inclusions, it fails to capture the full field subtleties of the development of accumulated plastic strain away from the inclusion. This would require a significant extension of the model to include more sophisticated crystal plasticity models that include length scale hardening terms and precise description of the local microstructure (i.e. grain shape and crystal orientation), for example as developed by Zhang et al. [30]. This effort is underway and will be presented in a subsequent paper.

4. Discussion

In this paper, we have used measurements of the distribution and development of effective strain (HR-DIC), microstructure (EBSD) and GND density (HR-EBSD) to understand crack initiation and microstructurally sensitive short crack growth. These correlative measurements have enabled us to quantitatively assess the relative contributions of these fields around an inclusion within a nickel-based superalloy matrix. Interrogation of these full field surface measurements and a geometrically faithful isotropic elastic finite element analysis provide us with mechanistic insight on the relative merits of different crack initiation metrics.

Deformation patterning and crack initiation is dependent on the loading mode and initial microstructure. The nickel-based sample has been prepared explicitly to explore the effect of non-metallic inclusions on crack initiation, and this is why the defect was placed near the edge of the tensile fibre of the three point bend test. The sample was subsequently heat treated to clean up any residual deformation and reduce any residual stresses, which from analysis

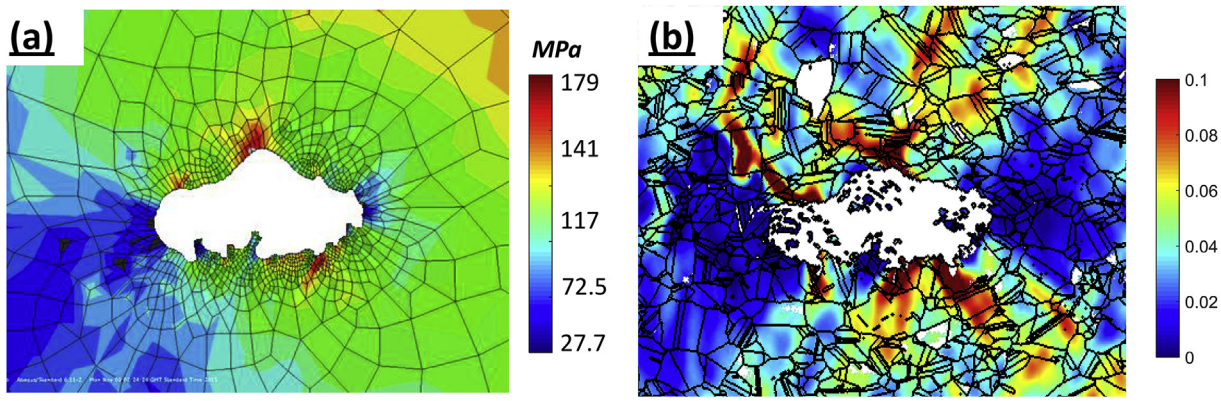

Fig. 10. (a) Finite element analysis of the max shear stress distribution at the inclusion. The non-metallic inclusion (E = 50 GPa, v = 0.31) was considered to be less stiff than the nickel matrix (E = 200 GPa, v = 0.31). (b), the effective strain map overlaid with grain boundary map determined by HR-DIC and EBSD respectively.

of the initial HR-EBSD maps (Fig. 5 (c)) has been largely achieved. In particular, the initial state of the nickel sample has very low dislocation density due to the heat treatment, as seen in Fig. 5 (c). However, accumulation of dislocations can still be found near the inclusion. This is due to the difference in thermal expansion coefficients of the non-metallic inclusion and the nickel matrix. Upon cooling, this difference leads to local plasticity generated around the inclusion, consistent with findings previously reported [Karamched et al. [45] and Zhang et al. [40]].

The behaviour of the material under plastic deformation adds to this existing microstructure, and a new patterning of GND density forms, as seen in Fig. 5 (f). In this study, we only monitored total deformation gradient (effective strain) as a function of increasing load and captured GND density only at the beginning and end of the experiment. In the previous study by Jiang et al. [18], the dislocation structure measured by HR-EBSD formed in the first loading cycle was relatively stable, developing slightly due to cyclic ratcheting. In low cycle fatigue and tensile loading of nickel-based superalloys at room temperature, patterning of GND density is principally determined by the local microstructure and loading configuration near the yield point. Increasing plastic strain results most strongly in the development of the existing pattern, increasing the magnitude of the dislocation density at each point. This enables us to assume that the shape of the dislocation structure during loading is correlated very strongly with the fields observed in Fig. 5 (f), once the test is concluded and the DIC patterning is removed to enable HR-EBSD measurements.

Development of the in-plane effective plastic strain, measured with HR-DIC, reveals that the distributions of plastic strain are created very early in the mechanical test and their strength develops as the load is increased. This is similar to observations of the evolution of stored GND density measured previously [18]. This confirms that the stored dislocation structure and dislocation slipping paths are determined by the local microstructure, which will not vary significantly by increasing deformation. Similar findings were also reported by other researchers using HR-DIC to address various micromechanical problems [20,24–26,33,46–48]. Observations that strain patterning is controlled principally by the initial microstructural configuration has a significant impact on how to understand materials deformation and engineer new materials. In this material system, constraint due to the inclusion, triple junctions and geometric features is likely to play a more important role in controlling local slip accumulation, rather than the generation of a significant local hardening which could lead to new slip paths forming. This has to be considered with care, as we do observe micro-cracks forming which is the ultimate form of deformation mode before failure of the complete microstructure. These crack positions are clearly influenced by the in-plane effective plastic slip and microstructure, as well as the stored GND density.

One of the key novelties of this paper is to experimentally obtain the GND density and effective strain maps on the same region of interest and to progressively track the development of effective plastic strain during deformation.

Analysis of GND density is necessarily indirect using HR-EBSD and Nye's analysis. In brief, the closure failure associated with a Burgers circuit is measured using the lattice rotation gradients (i.e. components of Curl F^e, neglecting the elastic strain gradients) and this is directly related to the GND density through the Nye tensor (full details of the method can be found here [37]). The presence of a wall of GNDs is directly related to a plastic strain gradient, but as observed by Jiang et al. [23], not all plastic strain gradients result in a stored GND density. In particular, in a (relatively) unconstrained single slip, the glide of dislocations on a discreet slip plane results in a plastic strain gradient and progressively accumulating continuum rotations, but as the dislocations are not stored within the lattice, there is not an accumulation of GNDs. Deformation in a polycrystal is likely to be a combination of relatively unconstrained single slip, e.g. single slip may be found within the centre of grains, and more constrained, e.g. due to the presence of grain boundaries, triple junctions and the presence of multiple slip systems. This is why it is impossible to directly correlate the accumulated in-plane effective strain with the GND density distribution for each point within our maps (i.e. with very high spatial resolution), as illustrated in Fig. 5 (e) and (f). Point based correlation of these two fields was plotted in Fig. 9, and this confirms difficulties in relating local accumulated strain with local values of high GND density (and related proxy metrics such as the Kernel Average Misorientation, or KAM). This observation is complementary to prior work by Jiang et al. [49] who studied the averaged evolution of plastic strain and the average increase in GND density. In those uniaxially strained polycrystalline oxygen free high conductivity copper samples, there was a direct correlation of the work hardening to statistical measurements of the GND density, through a simple Taylor equation, and in particular, it was found that an increase in flow stress correlated with the square root of the geometric mean of the GND density. The subtle difference of prior success at matching the mean GND density correlating with the average response of the polycrystal and the current difficulties linking local GND density and accumulated plastic strain is not to be overlooked.

Moving beyond plasticity and towards the main objective of this work, we focus on crack initiation and microstructurally short crack

growth near the non-metallic inclusion. Firstly, we note that the micro-crack– inclusion interactions within the present work are different to the non-metallic inclusion crack nucleation study by Zhang et al. [20], as in the present work cleavage occurred within the matrix and there was limited particle-matrix decohesion. This enables us to focus on identifying the local Ni-microstructure and dislocation effects on micro-crack nucleation.

Based on the HR-DIC measurement in Fig. 6, we can see that crack nucleation sites have the highest accumulated plastic slip associated with them. It seems to be necessary to have sufficient plastic strain to allow new cracked surfaces to be formed. This implies that crack formation follows plastic strain exhaustion. Furthermore, the local progressive development of plastic strain is modulated by local strain hardening, typically due to back stresses associated with the accumulation of dislocation density (both GNDs, as measured here, and also due to the presence of SSDs, which are more difficult to measure).

Next, we consider Stroh's model which correlates pile-ups of dislocations with an increase in the shear stress and subsequent crack nucleation. Our results, shown in (c), reveal that high dislocation density sites are not limited to cracking sites, as many of the areas of high GND density are located within the matrix interior and away from the inclusion. This implies that a crack nucleation criterion based solely on consideration of GND density is inappropriate certainly in the present nickel-based superalloy under study.

The plastic strain fracture model represents a mechanistic 'bound' on performance, i.e. in the limit where plasticity does not affect fracture initiation and microstructurally sensitive short crack growth, and Stroh's model represent an upper bound where the stored dislocation content exclusively controls crack formation. In many material systems, such as the nickel-based superalloy studied here, it is likely that there are contributions from both the stored energy and local dislocation structure. This motivates our testing of Dunne's approach, noting that in the experiments here we have to make some simplifying approximations such as how much plastic work correlates with stored energy (assumed to be 5% here) used to open the crack, as well as ignoring the SSD accumulation associated with the stored energy volume. In light of these simplifications, it is remarkable how well the crack nucleation and growth correlates with experimental observations.

As this is a ductile material, a combination of the stored energy rate and the stored dislocation density merits testing of Dunne's criterion. This has implicit microstructural length scale dependence (GND density) and also considers the potential for the stored energy, in order to open up a crack. Our testing of this criterion is limited, as only six cracks were explored and the macroscopic stress state, rather than the local microstructural stress state under load, was considered. However, within the scope of this limitation, it performed well as seen in Fig. 8(d).

Our local correlation between cracks and microstructure, using these sophisticated experimental tools, reveals interesting features such as in Fig. 7, where GND walls were formed ahead of the micro-crack tips. These GND walls may play a critical role to provide local hardening to blunt crack tip and slow down the crack propagation rate [17,50]. These GNDs seems to have dual roles in a micro-fracture process: (1) providing local stress amplifications to drive cracking; (2) shear stress driven blunting as suggested by the early nano-scale crack tip study by Kelly et al. [51] and Rice and Thomson [52]. Unfortunately, this highlights the multi-scale complexity of microstructurally sensitive cracking in ductile materials.

Furthermore, we see clear evidence of microstructurally sensitive short crack growth as micro-cracks in Fig. 3 follow the trace of slip lines at the free surface. This implies that nickel-based fcc crystal structure is prone to shear stress driven ductile fracture, and the critical shear stress to initiate dislocation slip is considerably lower than the critical tensile stress to break atomic bonds [51]. This is supported by the simple FE elastic analysis, shown in Fig. 10 (a), which shows that locations of these micro-cracks invariably have the highest max shear stress, and in the relatively symmetric fcc material this will result in comparatively easy crystal slip.

From the observations within this manuscript, we anticipate that crack initiation and short crack growth are controlled by the following mechanism:

(1) There is a resolved shear stress concentration at potential micro-crack sites, evidenced by localised plastic deformation observed in Fig. 5 (e).
(2) There is significant plastic strain variation within grains, due to the local strain gradient, and this generates a large number of GNDs. Meanwhile these GNDs provided hardening for the material locally, which increased the local critical resolved shear stress for dislocations to slip.
(3) The local stress increases the elastic stored energy. This is also combined with the increase in dislocation based stored energy. Furthermore, there is a local evolution of plastic work, due to dislocation slip, and this requires plastic dissipation.
(4) Stored energy can be dissipated through crack nucleation, perhaps where further dislocation slip is exhausted due to the accumulation of sessile dislocation debris (both GNDs and SSDs).
(5) Nucleated cracks, with an appropriate driving force, propagate typically along slip planes, resulting in microstructurally short crack growth. This driving force may be blunted however through the dissipation of stored energy as GNDs are formed ahead of the crack and cause blunting.

The role of stored energy, local blunting and the rising stresses around the inclusion are clearly interlinked. From an experimental point of view, it would be useful if the GND structure has a significant role and we observe that the GND structure is rather prominent in this study (Fig. 5 (f)). One driver is that it can be measured with relative ease using EBSD at a microstructural length scale. If GND density is indeed significant, then more insights might be provided to other intriguing phenomena. For example, for A533B weld metals, the size of the inclusions that initiated failure depends on loading histories [53]. The warm-load-cool process has significantly improved fracture toughness and fatigue life over a warm-load-unload-cool process. The understanding based on this study suggests that during the warm-load-cool process a GND network was generated and maintained through the cooling stage. This pre-existing GND network was subsequently subjected to further plastic deformation. As a result of the newly formed GND structure, crack nucleation might be more effectively blunted, and the distribution of stress and strain may be more uniform. In addition, this might be the same reason for the increase of sheet metal formability through non-proportional strain paths [54], in which several layers of dislocations structure were overlapped.

Finally, from an industrial perspective, to increase fracture toughness it is necessary to reduce local perturbations of the stress field. From the simple elastic FE modelling, the roughness of the inclusion plays a significant role, with the stress varying hugely from sharp corners to smooth edges. This is consistent with early experimental studies on Aluminium 7475 and weld steel in which the shape of inclusions was found to be very important for determining fatigue crack growth rate [55]. Furthermore, the effects of inclusion on low cycle fatigue life at different elevated temperatures and under peened and unpenned conditions seem to be critical [2]. The understanding of these effects would allow more accurate in-service low cycle fatigue life to be predicted.

5. Conclusion

This paper presents a correlative HR-EBSD, HR-DIC and EBSD study of crack nucleation in nickel-based superalloys loaded with increasing load using three-point bending. The initial and final distributions of GND density maps were obtained by the HR-EBSD technique, while the progressive variation in effective (total) strain distribution at the same area was captured using HR-DIC. The combination of these two deformation characterisation techniques at local grain scale provided valuable information to reveal the micro-crack forming mechanisms. The following conclusions can be drawn from this study:

- Six micro-cracks were observed at the interface of the inclusion and nickel matrix. Four of them were nucleated within the grains, and the other two were generated at grain boundaries.
- The structure of effective strain distribution was found to be set at the beginning of plasticity. Further increases in plasticity only lead to polarizing more the high and low strain distributions within the structure but maintains the general heterogeneous distribution of plastic strain across the field studied.
- Near the crack nucleation sites, the GND density was found to be high. However, the high GND density points were found to be scattered in the map and were not limited to crack nucleation sites.
- GND constituted dislocation walls were found to be in front of crack tips. It was speculated that GND wall structure will have a significant influence on materials toughness e.g. crack nucleation and propagation by blunting the crack tip and altering the stored energy state.
- The geometry of the inclusion plays a significant role in raising local stress, but the nucleation of cracks is not exclusively dependant on this, and a major role is also played by local GND accumulation and plastic slip. Furthermore, microstructurally sensitive short crack growth was also observed.

Acknowledgements

Much appreciated is the strong support received from AVIC Beijing Institute of Aeronautical Materials (BIAM). The research was performed at the AVIC Centre for Materials Characterisation, Processing and Modelling at Imperial College London. Authors also appreciate strong supports from Rolls-Royce, EPSRC (grant EP/L025213/1), Royal Academy of Engineering for T.B.B.'s RAEng Research Fellowship and F.P.E.D.'s RAEng Research Chair.

References

[1] R.C. Reed, The Superalloys: Fundamentals and Applications, Cambridge university press, 2008.
[2] E.S. Huron, P.G. Roth, The influence of inclusions on low cycle fatigue life in a P/M nickel-base disk superalloy, Superalloys 1996 (1996) 359–368.
[3] D. Chang, D. Krueger, R. Sprague, Superalloy powder processing, properties and turbine disk applications, Superalloys 1984 (1984) 245–273.
[4] J. Hyzak, I. Bernstein, The effect of defects on the fatigue crack initiation process in two P/M superalloys: Part I. Fatigue origins, Metall. Trans. A 13 (1982) 33–43.
[5] T. Gabb, J. Telesman, P. Kantzos, P. Bonacuse, R. Barrie, Initial Assessment of the Effects of Nonmetallic Inclusions on Fatigue Life of Powder-metallurgy-processed Udimet (TM) 720, 2002.
[6] P.J. Bonacuse, P. Kantzos, J. Telesman, T. Gabb, R. Barrie, Modeling ceramic inclusions in powder metallurgy alloys, in: Fatigue 2002: Proceedings of the Eighth International Fatigue Congress, vol. 2, 2002, pp. p.1339–1346.
[7] T. Denda, P.L. Bretz, J.K. Tien, Inclusion size effect on the fatigue crack propagation mechanism and fracture mechanics of a superalloy, Metall. Trans. A 23 (1992) 519–526.
[8] M. Shenoy, R. Kumar, D. McDowell, Modeling effects of nonmetallic inclusions on LCF in DS nickel-base superalloys, Int. J. Fatigue 27 (2005) 113–127.
[9] K.O. Findley, A. Saxena, Low cycle fatigue in Rene 88DT at 650 C: crack nucleation mechanisms and modeling, Metallurgical Mater. Trans. A 37 (2006) 1469–1475.
[10] R.C. Reed, K.A. Green, P. Caron, T.P. Gabb, M.G. Fahrmann, E.S. Huron, S.A. Woodard, Microstructural Conditions Contributing to Fatigue Variability in P/M Nickel-base Superalloys, 2008.
[11] M.D. Sangid, The physics of fatigue crack initiation, Int. J. fatigue 57 (2013) 58–72.
[12] J. Miao, T.M. Pollock, J.W. Jones, Microstructural extremes and the transition from fatigue crack initiation to small crack growth in a polycrystalline nickel-base superalloy, Acta Mater. 60 (2012) 2840–2854.
[13] D. McDowell, F.P.E. Dunne, Microstructure-sensitive computational modeling of fatigue crack formation, Int. J. fatigue 32 (2010) 1521–1542.
[14] D. Fairchild, D. Howden, W. Clark, The mechanism of brittle fracture in a microalloyed steel: Part I. Inclusion-induced cleavage, Metallurgical Mater. Trans. A 31 (2000) 641–652.
[15] J. Lautridou, A. Pineau, Crack initiation and stable crack growth resistance in A508 steels in relation to inclusion distribution, Eng. Fract. Mech. 15 (1981) 55–71.
[16] G. Hahn, A. Rosenfield, Metallurgical factors affecting fracture toughness of aluminum alloys, Metall. Trans. A 6 (1975) 653–668.
[17] J.F. Knott, A.R. Boccaccini, The fracture mechanics-microstructure linkage, Mech. Mater. Fundam. Link. (1999) 399–427.
[18] J. Jiang, J. Yang, T. Zhang, F.P.E. Dunne, T.B. Britton, On the mechanistic basis of fatigue crack nucleation in Ni superalloy containing inclusions using high resolution electron backscatter diffraction, Acta Mater. 97 (2015) 367–379.
[19] Tiantian Zhang, Jun Jiang, Ben Britton, Barbara Shollock, F.P.E. Dunne, Crack nucleation using combined crystal plasticity modelling, HR-DIC and HR-EBSD in a superalloy containing non-metallic inclusions under fatigue, Proc. R. Soc. A 472 (2016), 20160037, The Royal Society.
[20] T. Zhang, J. Jiang, B.A. Shollock, T.B. Britton, F.P.E. Dunne, Slip localization and fatigue crack nucleation near a non-metallic inclusion in polycrystalline nickel-based superalloy, Mater. Sci. Eng. A 641 (2015) 328–339.
[21] B. Pan, K. Qian, H. Xie, A. Asundi, Two-dimensional digital image correlation for in-plane displacement and strain measurement: a review, Meas. Sci. Technol. 20 (2009) 062001.
[22] G. Vendroux, W. Knauss, Submicron deformation field measurements: Part 2. Improved digital image correlation, Exp. Mech. 38 (1998) 86–92.
[23] J. Jiang, T. Zhang, F.P.E. Dunne, T.B. Britton, Deformation compatibility in a single crystalline Ni superalloy, Proc. R. Soc. A 472 (2016) 20150690. The Royal Society.
[24] A.D. Kammers, S. Daly, Self-assembled nanoparticle surface patterning for improved digital image correlation in a scanning electron microscope, Exp. Mech. 53 (2013) 1333–1341.
[25] J. Stinville, M. Echlin, D. Texier, F. Bridier, P. Bocher, T. Pollock, Sub-grain scale digital image correlation by electron microscopy for polycrystalline materials during elastic and plastic deformation, Exp. Mech. 56 (2016) 197–216.
[26] F. Di Gioacchino, J.Q. da Fonseca, Plastic strain mapping with sub-micron resolution using digital image correlation, Exp. Mech. 53 (2013) 743–754.
[27] J.F. Nye, Physical Properties of Crystals, 1957.
[28] N. Fleck, M. Ashby, J. Hutchinson, The role of geometrically necessary dislocations in giving material strengthening, Scr. Mater. 48 (2003) 179–183.
[29] L. Evers, D. Parks, W. Brekelmans, M. Geers, Crystal plasticity model with enhanced hardening by geometrically necessary dislocation accumulation, J. Mech. Phys. Solids 50 (2002) 2403–2424.
[30] M. Ashby, The deformation of plastically non-homogeneous materials, Philos. Mag. 21 (1970) 399–424.
[31] H. Gao, Y. Huang, Geometrically necessary dislocation and size-dependent plasticity, Scr. Mater. 48 (2003) 113–118.
[32] F.P.E. Dunne, R. Kiwanuka, A.J. Wilkinson, Crystal plasticity analysis of micro-deformation, lattice rotation and geometrically necessary dislocation density, Proc. R. Soc. A 468 (2012) p.2509–2531. The Royal Society.
[33] M. Calcagnotto, D. Ponge, E. Demir, D. Raabe, Orientation gradients and geometrically necessary dislocations in ultrafine grained dual-phase steels studied by 2D and 3D EBSD, Mater. Sci. Eng. A 527 (2010) 2738–2746.
[34] T. Ohashi, Finite-element analysis of plastic slip and evolution of geometrically necessary dislocations in fcc crystals, Philos. Mag. Lett. 75 (1997) 51–58.
[35] A.J. Wilkinson, G. Meaden, D.J. Dingley, High-resolution elastic strain measurement from electron backscatter diffraction patterns: new levels of sensitivity, Ultramicroscopy 106 (2006) 307–313.
[36] T.B. Britton, A.J. Wilkinson, Stress fields and geometrically necessary dislocation density distributions near the head of a blocked slip band, Acta Mater. 60 (2012) 5773–5782.
[37] W. Pantleon, Resolving the geometrically necessary dislocation content by conventional electron backscattering diffraction, Scr. Mater. 58 (2008) 994–997.
[38] D. Hull, D.J. Bacon, Introduction to Dislocations, Butterworth-Heinemann, 2001.
[39] A.J. Wilkinson, D. Randman, Determination of elastic strain fields and geometrically necessary dislocation distributions near nanoindents using electron back scatter diffraction, Philos. Mag. 90 (2010) 1159–1177.
[40] T. Zhang, D.M. Collins, F.P.E. Dunne, B.A. Shollock, Crystal plasticity and high-resolution electron backscatter diffraction analysis of full-field polycrystal Ni superalloy strains and rotations under thermal loading, Acta Mater. 80 (2014) 25–38.
[41] A.N. Stroh, A theory of the fracture of metals, Adv. Phys. 6 (1957) 418–465.
[42] V. Wan, D. MacLachlan, F. Dunne, A stored energy criterion for fatigue crack

nucleation in polycrystals, Int. J. Fatigue 68 (2014) 90–102.
[43] V. Wan, J. Jiang, D. MacLachlan, F.P.E. Dunne, Microstructure-sensitive fatigue crack nucleation in a polycrystalline Ni superalloy, Int. J. Fatigue 90 (2016) 181–190.
[44] F. Roters, P. Eisenlohr, L. Hantcherli, D.D. Tjahjanto, T.R. Bieler, D. Raabe, Overview of constitutive laws, kinematics, homogenization and multiscale methods in crystal plasticity finite-element modeling: theory, experiments, applications, Acta Mater. 58 (2010) 1152–1211.
[45] P.S. Karamched, A.J. Wilkinson, High resolution electron back-scatter diffraction analysis of thermally and mechanically induced strains near carbide inclusions in a superalloy, Acta Mater. 59 (2011) 263–272.
[46] F. Di Gioacchino, J.Q. da Fonseca, An experimental study of the polycrystalline plasticity of austenitic stainless steel, Int. J. Plast. 74 (2015) 92–109.
[47] J. Stinville, N. Vanderesse, F. Bridier, P. Bocher, T. Pollock, High resolution mapping of strain localization near twin boundaries in a nickel-based superalloy, Acta Mater. 98 (2015) 29–42.
[48] J.D. Carroll, W.Z. Abuzaid, J. Lambros, H. Sehitoglu, On the interactions between strain accumulation, microstructure, and fatigue crack behavior, Int. J. Fract. 180 (2013) 223–241.
[49] J. Jiang, T.B. Britton, A.J. Wilkinson, Evolution of dislocation density distributions in copper during tensile deformation, Acta Mater. 61 (2013) 7227–7239.
[50] D. Hull, D.J. Bacon, Introduction to Dislocations, Elsevier, 2011.
[51] A. Kelly, W. Tyson, A. Cottrell, Ductile and brittle crystals, Philos. Mag. 15 (1967) 567–586.
[52] J.R. Rice, R. Thomson, Ductile versus brittle behaviour of crystals, Philos. Mag. 29 (1974) 73–97.
[53] P. Reed, J. Knott, An investigation of the warm prestressing (WPS) effect in A533B weld metal, Fatigue & Fract. Eng. Mater. Struct. 15 (1992) 1251–1270.
[54] A.B. Da Rocha, F. Barlat, J. Jalinier, Prediction of the forming limit diagrams of anisotropic sheets in linear and non-linear loading, Mater. Sci. Eng. 68 (1985) 151–164.
[55] J. Knott, J. King, Fatigue in metallic alloys containing non-metallic particles, Mater. Des. 12 (1991) 67–74.